JOURNAL OF SOLID STATE CHEMISTRY 135, 201–209 (1998)
ARTICLE NO. SC977620

# An Electron Diffraction Study of Short-Range Order in the $(1-x)Bi_2O_3 \cdot xCaO$ $\gamma$-Type Solid Solution and Its Relationship to Low-Temperature $Ca_4Bi_6O_{13}$

Ann-Kristin Larsson and Ray Withers[1]

*Research School of Chemistry, Australian National University, Canberra, ACT 0200, Australia*

Received June 10, 1997; in revised form September 12, 1997; accepted September 15, 1997

**The body centered cubic ($a \sim 4.26$ Å) $\gamma$-type solid solution (ss$\gamma$) phase $(1-x)Bi_2O_3 \cdot xCaO$ ($\sim 0.50 < x < \sim 0.60$ at $\sim 820°C$) was investigated by electron diffraction. Instead of finding evidence for additional Bragg reflections at $\mathbf{G} \pm \mathbf{a}^*$ as previously assumed attempting to interpret powder neutron diffraction data (Gruber *et al.*, *J. Solid State Chem.* 108, 250–252, 1994), localized diffuse scattering was detected and described by $\mathbf{G} \pm \mathbf{q}$, where $\mathbf{q} \approx 0.2\langle 211 \rangle_\gamma^*$ is a (diffuse) modulation wave vector. A crystal structural relationship between the cation arrays in the ss$\gamma$ phase and the low-temperature line phase, $Ca_4Bi_6O_{13}$ (LT), was established. The unit cell of the LT phase can be expressed as $\mathbf{a}_{LT} = \mathbf{a}_\gamma - \mathbf{c}_\gamma$, $\mathbf{b}_{LT} = \frac{5}{3}(\mathbf{a}_\gamma - 2\mathbf{b}_\gamma + \mathbf{c}_\gamma)$ and $\mathbf{c}_{LT} = \frac{1}{2}(\mathbf{a}_\gamma + \mathbf{b}_\gamma + \mathbf{c}_\gamma)$. From the cation ordering in the LT phase and the reciprocal space relation $2\mathbf{b}_{LT}^* = 0.2\langle 1\bar{2}1 \rangle_\gamma^* \approx \mathbf{q}$, the localized diffuse scattering in the ss$\gamma$ phase was linked to cation ordering into layers perpendicular to $\langle 1\bar{2}1 \rangle_\gamma$.** 

## INTRODUCTION

Much work has been devoted over a considerable period of time to the remarkable oxygen ion and electrical transport properties of a range of ternary bismuth oxide phases (1–4). Such phases are frequently highly conductive when in the form of solid solution phases at elevated temperatures but often undergo phase transitions upon cooling at which desirable transport properties can change by several orders of magnitude (1, 4).

One such ternary bismuth oxide phase is the body centered cubic (bcc; $a \sim 4.26$ Å at 870°C), so-called $\gamma$-type solid solution phase (the ss$\gamma$ phase) in the $(1-x)Bi_2O_3 \cdot xCaO$ system. It is reported to exist over the composition range $\sim 0.50 < x < \sim 0.60$ for temperatures greater than $\sim 820°C$ (5). This $\gamma$-type ternary bismuth oxide phase was initially reported for $M = Cd$ (6) but has since also been reported for $M = Sr$ (7), Pb (8), and Na, K, Mn, and Ba (9). The crystal structure of the Cd compound was reported as being of anti-$\alpha$-AgI type, space group $Im3m$ with Bi and Cd being statistically distributed in the (2*a*) sites (no superstructure reflections could be detected in overexposed Weissenberg photographs) and with oxygen partially occupying the (12*d*) sites (4). The conductivity of this anti-$\alpha$-AgI type phase at elevated temperatures has been attributed to mobility of oxygen ions within an immobile cation framework and is thus considered to be the perfect counterpart to $\alpha$-AgI itself where conductivity is due to mobile silver ions within an immobile anion framework (4).

In the case of $M = Sr$, Bi/Sr cation ordering has been reported as being responsible for the existence of a high-temperature tetragonal superstructure phase ($I4/mmm$, $a \sim 13.24$, $c \sim 4.26$ Å) which only transforms into the disordered bcc, ss$\gamma$ phase just prior to melting (4, 7). Rather more recently, Delicat *et al.* (9) mentioned that electron diffraction patterns (EDPs) from the $M = Ba$, ss$\gamma$ phase show weak incommensurate satellite reflections in addition to the set of strong Bragg reflections typical of the bcc lattice. They could not find such additional reflections in EDPs from the $M = Ca$ ss$\gamma$ phase.

Gruber *et al.* (10) studied quenched specimens of the $M = Ca$ ss$\gamma$ phase at $x = 0.57$ via powder neutron diffraction (PND) at 8 K. In addition to a set of strong Bragg reflections consistent with an $Im3m$ ($a = 4.246$ Å at 8 K) average structure (hereafter labeled $\mathbf{G}_\gamma$), a relatively strong diffuse background scattering which appeared to peak at certain specific values of $2\theta$ was observed. Based on an interpretation of these few weak broad peaks observed in the PND data as representing additional Bragg reflections (indexed as 100, 111, 210, and 221/300) broadened by small particle size effects, the structure was described as being composed of an $Im3m$ ($a = 4.246$ Å) cation array (with the cations fully occupying the (2*a*) sites at 000) and an $R3m$ ($a = 4.246$ Å, $\alpha = 90°$) partially occupied oxygen ion array (with the oxygens partially occupying the (6*c*) sites therein at 0.32, 0.96, 0.54). Such an interpretation requires the existence of weak diffuse peaks at $\mathbf{G}_\gamma \pm \mathbf{a}^*$ (i.e., reflections *hkl*

[1] To whom correspondence should be addressed.



0022-4596/98 $25.00

with $h + k + l$ odd) with respect to the strong Bragg reflections of the underlying *Im*3*m* average structure.

While the existence of a strong (and reasonably sharply peaked) diffuse background in the PND experiments (10) is an important observation, the distribution of this diffuse intensity in reciprocal space cannot be determined reliably by a powder diffraction method. Electron diffraction (ED), by contrast, is ideally suited to map out the distribution of weak, diffuse features of reciprocal space due to the strong interaction of electrons with matter and to the ease with which tilted series of two-dimensional reciprocal space sections from single crystal regions can be obtained. The initial purpose of this contribution was to investigate via ED whether the assumption of Gruber *et al.* (10) with regard to the existence of weak diffuse peaks at $\mathbf{G}_\gamma \pm \mathbf{a}^*$ with respect to the underlying *Im*3*m* average structure was or was not valid.

Crystal structure relationships between distinct but related phases potentially give useful insight into structure–property relationships. A subsidiary purpose therefore was to investigate whether or not there was any structural relationship between the higher temperature ss$\gamma$ phase and two previously reported low-temperature line phases whose compositions are reported to fall within the composition range of existence of the ss$\gamma$ phase (5)—namely $Ca_4Bi_6O_{13}$ and $CaBi_2O_4$.

In this paper attention is drawn to a relationship between the cation packing (11) of the high-temperature $(1 - x)$ $Bi_2O_3 \cdot x$CaO, $\sim 0.55 < x < 0.60$, ss$\gamma$ phase and that of the related low-temperature line phase, LT-$Ca_4Bi_6O_{13}$. The establishment of such a relationship leads to the conclusion that the diffuse scattering observed for the quenched ss$\gamma$ phase is not, as previously reported, due to a lowering in symmetry of the oxygen ion array. Rather, it would appear to be connected with the existence of short-range metal ion ordering within the quenched ss$\gamma$ phase.

## EXPERIMENTAL METHODS

Samples were prepared by grinding $Bi_2O_3$ (Atomergic Chemetals Co., 99.999%) and $CaCO_3$ (Halewood Chemicals LTD, 99.999%) in the ratios 3:4 or 1:1. The samples were calcined at 750°C for 2–4 h in open gold tubes and then melted for 5 min at 1000°C (1000 or 950°C for the 1:1 sample) prior to quenching in water (10). The samples were then reground and heat treated appropriately. PXRD data were collected using a Guinier–Hägg camera with monochromated Cu$K\alpha_1$ radiation. Si (NBS No. 640) was added as internal standard for the determination of unit cell dimensions. Electron diffraction patterns (EDPs) were recorded using a JEOL 100CX transmission electron microscope (TEM). The specimens were prepared by crushing and dispersing onto holey-carbon coated copper grids.

## RESULTS

### *Initial Powder XRD Investigation*

Samples with the nominal composition of the two known low-temperature line phases, $CaBi_2O_4$ and $Ca_4Bi_6O_{13}$, were prepared as they fall within the composition range of the reported ss$\gamma$ phase field (5). Quenching samples of $Ca_4Bi_6O_{13}$ from above 850°C gave the lemon colored ss$\gamma$ phase (cI, $\mathbf{a} = 4.2523(3)$ Å) with no indication of impurity phases. Quenching samples with the composition $CaBi_2O_4$ from above 850°C, however, gave specimens consisting of about 20% ss$\alpha_1$ (cF, $\mathbf{a} \approx 5.63$) and 80% ss$\gamma$. The ss$\gamma$ region therefore seems to be slightly narrower than suggested (5); i.e., the phase border at the $Bi_2O_3$ rich side of the ss$\gamma$ region should be shifted to a $Bi_2O_3$ content slightly lower than 50 mol%.

The low-temperature line phase, LT-$Ca_4Bi_6O_{13}$ (lime colored), formed readily from the quenched sample of the same composition on heat treatment. Annealing the quenched samples for 10 min at 700°C was enough to complete the phase transition. This rapid formation of the LT phase on annealing of the quenched ss$\gamma$ phase is significant and suggests a close structural relationship between the two phases. (Annealing the quenched samples for shorter periods of time or at lower temperatures within the temperature range of the LT-$Ca_4Bi_6O_{13}$ phase sharpened considerably the diffuse distribution characteristic of the quenched ss$\gamma$ phase—see, for example, Figs. 1 and 2). The samples of the LT phase used for ED investigations were annealed up to $3 \times 24$ h at 790°C in order to enhance crystallinity. The samples were free from any LT-$CaBi_2O_4$ lines confirming, as pointed out previously (12), the $Ca_4Bi_6O_{13}$ composition of this low-temperature line phase.

The quenched samples of nominal composition $CaBi_2O_4$ transformed much more sluggishly to the LT-$CaBi_2O_4$ phase (grey-beige); e.g., $2 \times 24$ h at 790°C transformed 95% of the sample. This supports the indications from the quenching experiment—namely that this composition is outside the homogeneity range of the ss$\gamma$ phase and that the LT-$CaBi_2O_4$ phase is not closely related to the ss$\gamma$ phase. The ED investigation was therefore concentrated on the relationship between the ss$\gamma$ and LT-$Ca_4Bi_6O_{13}$ phases.

### *Diffraction of ss$\gamma$*

In contrast with the assumption of Gruber *et al.* (10), no diffuse intensity could ever be observed at the $\mathbf{G} \pm \mathbf{a}^*$ positions of reciprocal space in appropriately oriented EDPs of the quenched ss$\gamma$ phase. Figure 1a, for example, shows an $\langle 001 \rangle_\gamma$ zone axis EDP of the quenched ss$\gamma$ phase. While there is very weak diffuse streaking along the $\langle 110 \rangle_{\gamma^*}$ directions of reciprocal space, there is clearly no diffuse peaking at the $hk0_\gamma$, $h + k = 2n + 1$, positions of reciprocal space. Figure 1c shows the equivalent $\langle 001 \rangle_\gamma$ zone axis EDP for

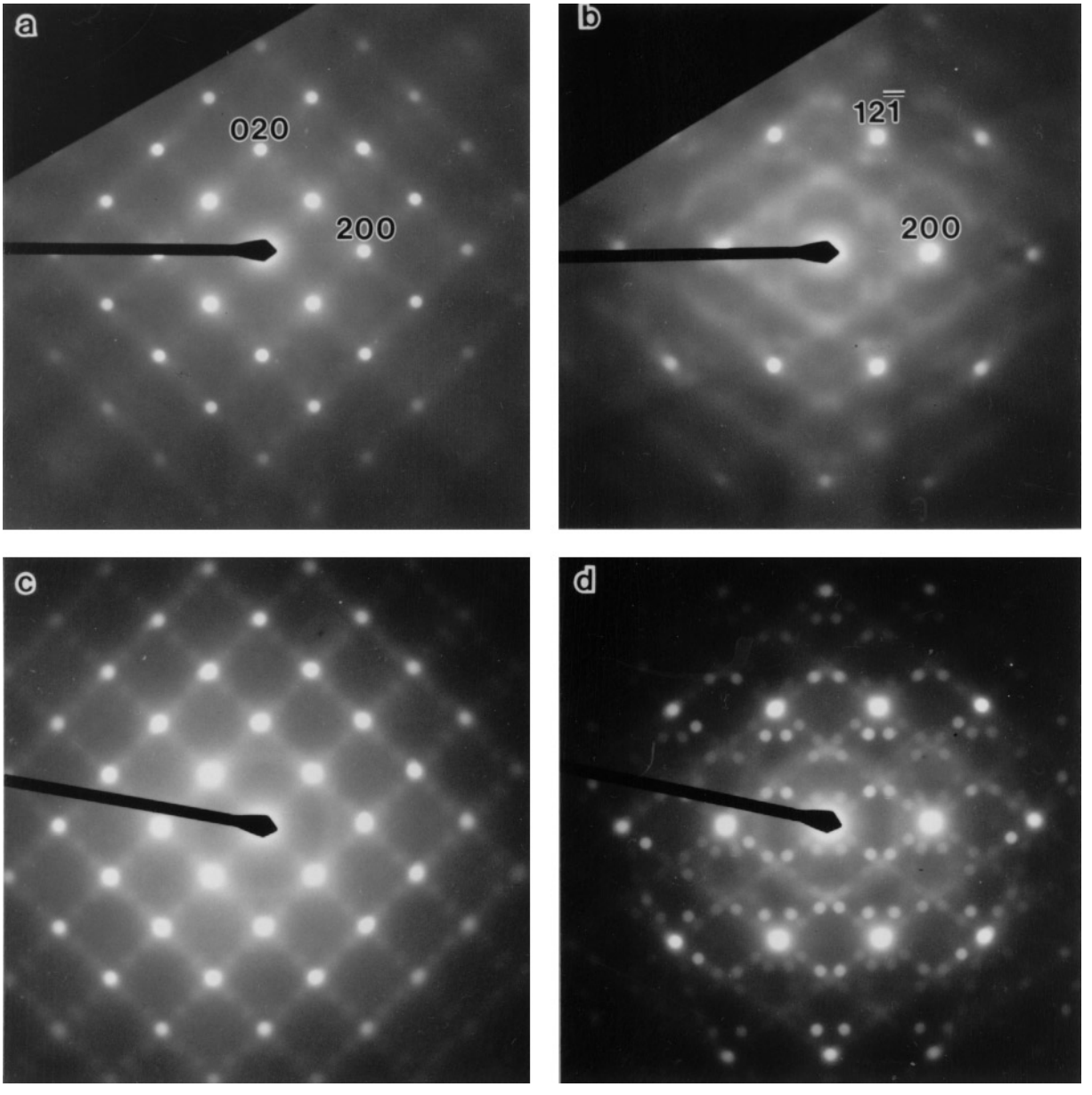


**FIG. 1.** (a) and (b) show EDPs from a quenched ss$\gamma$ phase along zone axes $\langle 001\rangle_\gamma$ and $\langle 012\rangle_\gamma$, respectively. The corresponding EDP for the same sample after additional annealing for 10 min at 500°C are shown in (c) and (d). There is no indication of intensity in $hkl$, $h+k+l=2n+1$. Instead, especially in (b) and (d), additional localized diffuse electron scattering is obvious. Most of this can be described with a modulation wave vector $\mathbf{q} \approx 0.2\langle 121\rangle^*$. This is clearer when comparing the intensity along $\langle 32\bar{1}\rangle_\gamma^*$ in (b) and (d) to the intensity along $\langle 32\bar{1}\rangle_\gamma^*$ in Fig. 2a and 2e.

a quenched ss$\gamma$ phase specimen which has been annealed at 500°C for 10 min to enhance and sharpen up the diffuse distribution characteristic of the quenched ss$\gamma$ phase. Again there is absolutely no hint of diffuse peaking at the $\mathbf{G} \pm \mathbf{a}^*$ positions of reciprocal space. (The EDPs of the annealed sample are always rather sharper than those of the as quenched samples and hence it is useful to refer to them to more easily appreciate the features of the EDPs of the quenched ss$\gamma$ phase. There are, however, some differences between the annealed samples and the as quenched samples, *vide infra*.)

On tilting from this $\langle 001\rangle_\gamma$ zone axis orientation, keeping $\langle 200\rangle_{\gamma^*}$ excited, a relatively strong, quite structured diffuse intensity distribution accompanying the strong Bragg reflections characteristic of the bcc average structure became apparent. Figure 1b, for example, shows an $\langle 012\rangle_\gamma$ zone axis EDP in which this localized diffuse scattering is relatively pronounced. Figure 1d shows the corresponding $\langle 012\rangle_\gamma$

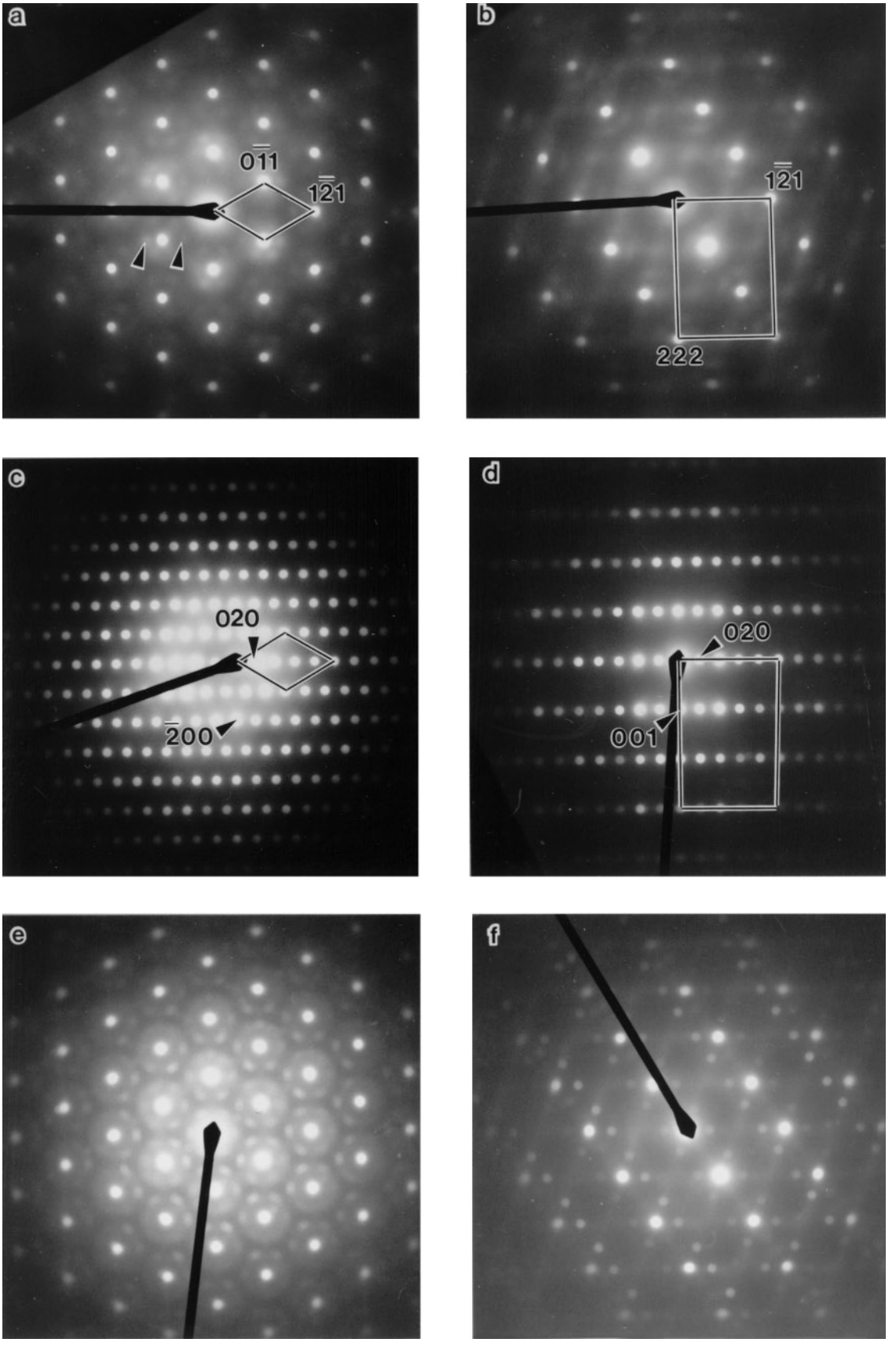
a
011
121
b
121
222
c
020
200
d
020
001
e
f

zone axis EDP for a quenched ss$\gamma$ specimen which has again been annealed at 500°C for 10 min. The quite pronounced blobs of diffuse intensity visible in Fig. 1b have sharpened considerably into apparent satellite reflections in Figure 1d. Note, however, that the diffuse streaking linking the blobs of diffuse intensity along the $\langle 321\rangle^*_\gamma$ directions of reciprocal space in Fig. 1b still remains in Fig. 1d. While the absolute intensity and sharpness of the diffuse distribution characteristic of the quenched ss$\gamma$ phase is clearly strongly dependent upon the degree of annealing (compare Fig. 1a with 1c and Fig. 1b with 1d), the location in reciprocal space and the basic shape of the additional scattering always remain similar.

When the quenched ss$\gamma$ specimen is aligned along or close to $\langle 111\rangle_\gamma$, diffuse peaks were always weakly, but clearly, visible at reciprocal lattice positions given by $\mathbf{H} = \mathbf{G}_\gamma \pm \mathbf{q}$, where $\mathbf{q} \sim 0.2\langle 1\bar{2}1\rangle^*_\gamma$ (see Fig. 2a). For the quenched ss$\gamma$ specimen annealed at 500°C for 10 min (see Fig. 2e), these diffuse peaks have sharpened considerably and appear to have split into two narrowly separated sets of satellite reflections at $\mathbf{G}_\gamma \pm \mathbf{q}_1$, where $\mathbf{q}_1 \sim 0.23\langle 1\bar{2}1\rangle^*_\gamma + \sim 0.04\langle \bar{1}01\rangle^*_\gamma$ and at $\mathbf{G}_\gamma \pm \mathbf{q}_2$, where $\mathbf{q}_2 \sim 0.23\langle 1\bar{2}1\rangle^*_\gamma - 0.04\langle \bar{1}01\rangle^*_\gamma$; i.e., the modulation wave vectors, although rather close, do not quite point along the $\langle 121\rangle^*_\gamma$ directions of reciprocal space.

At first glance, the $\langle 012\rangle_\gamma$ zone axis EDPs of the quenched specimen (see Figs. 1b and 1d) appear to show diffuse peaking in addition to the intensity present in the $\mathbf{G}_\gamma \pm \mathbf{q}$, $\mathbf{q} \sim 0.2\langle 1\bar{2}1\rangle^*_\gamma$, regions of reciprocal space. Most of this additional intensity, however, can be interpreted as originating from the $\mathbf{q} \approx 0.2\langle 211\rangle^*_\gamma$ set of modulation vectors provided all symmetry equivalent $\sim 0.2\langle 211\rangle^*_\gamma$ modulation wave vectors are taken into account. This is rather more readily appreciated by consideration of the corresponding $\langle 012\rangle_\gamma$ zone axis EDP of the quenched ss$\gamma$ specimen annealed at 500°C for 10 min (see Fig. 1d). In addition to satellite reflections at $\mathbf{G}_\gamma \pm \mathbf{q}$, $\mathbf{q} \sim 0.23\langle 1\bar{2}1\rangle^*_\gamma$, there also exist satellite reflections at $\mathbf{G}_\gamma \pm \mathbf{q}$, where $\mathbf{q} \sim 0.27\langle 321\rangle^*_\gamma$. Note, however, that $0.27\langle 321\rangle^*_\gamma = \langle 110\rangle^*_\gamma - 0.23\langle 12\bar{1}\rangle^*_\gamma + 0.04\langle 101\rangle^*_\gamma$ (see Fig. 2e). Thus the intensity distribution along the $\langle 321\rangle^*_\gamma$ directions of reciprocal space, e.g., between $\bar{2}00_\gamma$ and $12\bar{1}_\gamma$ in Figs. 1b and 1d, is clearly closely similar to that along $\langle 321\rangle^*_\gamma$ directions of reciprocal space in Figs. 2a and 2e.

Figure 2b shows a $\langle 10\bar{1}\rangle_\gamma$ zone axis EDP for the quenched ss$\gamma$ specimen and Fig. 2f shows the corresponding $\langle 10\bar{1}\rangle_\gamma$ zone axis EDP for the quenched ss$\gamma$ specimen annealed at 500°C for 10 min. Note that the $\langle 10\bar{1}\rangle_\gamma$ zone axis orientation is perpendicular to $\langle 111\rangle_\gamma$ (the zone axis orientation of Figs. 2a and 2e) but still has $\langle 1\bar{2}1\rangle^*_\gamma$ excited. Again note the presence of satellite reflections at $\mathbf{G}_\gamma \pm \mathbf{q}$, $\mathbf{q} \sim 0.23\langle 1\bar{2}1\rangle^*_\gamma$ in Fig. 2f (and diffuse blobs of intensity in $\mathbf{q} \sim 0.2\langle 1\bar{2}1\rangle^*_\gamma$ in the as quenched ss$\gamma$ phase in Fig. 2b). Rather than diffuse peaking at the $\mathbf{G}_\gamma \pm \mathbf{a}^*$ positions of reciprocal space as proposed by Gruber *et al.* (10), it is clear that the quenched ss$\gamma$ phase is characterized by diffuse peaking in the vicinity of the $\mathbf{G}_\gamma \pm \pm \mathbf{q}$, $\mathbf{q} \sim 0.2\langle 1\bar{2}1\rangle^*_\gamma$ regions of reciprocal space.

To confirm that the diffuse electron scattering observed in these samples was compatible with the diffuse neutron scattering observed previously (10), and hence that these samples were of the same phase, the $d$ values of the two reasonably sharp diffuse peaks of the previously reported PND data were measured and found to occur at $d \sim 4.28$ and 2.46 Å. These $d$ values are compatible with the strongest features of the diffuse electron scattering observed in the quenched ss$\gamma$ phase here (see arrows in Fig. 2a) and hence the ED patterns recorded seem to be entirely consistent with the previously reported neutron data. The question remains as to what sort of local ordering is responsible for the observed diffuse peaking in the vicinity of the $\mathbf{G} \pm \mathbf{q}$, $\mathbf{q} \sim 0.2\langle 1\bar{2}1\rangle_{\gamma^*}$ regions of reciprocal space in the quenched ss$\gamma$ phase. The rapid formation of the LT phase on annealing of the quenched ss$\gamma$ phase suggests that a close examination of the LT phase might well provide an explanation.

### *Diffraction of LT-$Ca_4Bi_6O_{13}$*

The crystal structure of LT-$Ca_4Bi_6O_{13}$ was recently reported (12) using unit cell parameters $\mathbf{a} = 5.937(1)$, $\mathbf{b} = 17.356(4)$, and $\mathbf{c} = 7.206(4)$ Å and space group symmetry *C2mm*. Rotation and precession photographs, as well as powder diffraction patterns, of LT-$Ca_4Bi_6O_{13}$ were reported as all being consistent with the presence of a strong subcell along $c^*$ ($c^* = \frac{1}{2}c^*_{\text{subcell}}$) implying the existence of a weak ($2 \times c_{\text{subcell}} = 2 \times 3.6$ Å) superstructure along the $c$ axis direction.

EDPs of LT-$Ca_4Bi_6O_{13}$ (see Figs. 2c and 2d) show a set of strong Bragg reflections (labeled $\mathbf{G}_{\text{LT}}$) fully consistent with the C-centered orthorhombic subcell of Parise *et al.* (12) and Roth *et al.* (13), i.e., $\mathbf{a}_{\text{LT}} = 5.9$, $\mathbf{b}_{\text{LT}} = 17.3$, and $\mathbf{c}_{\text{LT}} = 3.6$ Å, but not with the implied weaker satellite reflections at $\mathbf{G}_{\text{LT}} \pm \frac{1}{2}\langle 001\rangle^*$ (see, for example, Fig. 2d). Very weak

**FIG. 2.** Comparison between the reciprocal lattices of the ss$\gamma$ and the LT-$Ca_4Bi_6O_{13}$ phases. (a) and (b) show EDPs of the as quenched ss$\gamma$ phase, (c) and (d) of LT-$Ca_4Bi_6O_{13}$ phase while (e) and (f) is from the quenched ss$\gamma$ phase, annealed for 10 min at 500°C. The zone axes are; (a) $\langle 111\rangle_\gamma$, (b) $\langle 10\bar{1}\rangle_\gamma$, (c) $\langle 001\rangle_{\text{LT}}$, (d) $\langle 100\rangle_{\text{LT}}$, (e) $\langle 111\rangle_\gamma$, and (f) $\langle 10\bar{1}\rangle_\gamma$. The relation between the ss$\gamma$ and LT-$Ca_4Bi_6O_{13}$ EDPs have been emphasized by drawing the reciprocal lattice of a formal subcell in common for the two structures: (a) and (c) are oriented along the $c$ axis of this (hypothetical) hexagonal cell and (b) and (d) are oriented along $\langle 1\bar{1}0\rangle$ of this subcell. Note by comparing (a) and (b) to (c) and (d) how the reciprocal lattice of the LT phase may be expressed in terms of the reciprocal lattice of the average ss$\gamma$ cell and the modulation wave vector $\mathbf{q} = \frac{1}{5}[1\bar{2}1]^*_\gamma$; $2\mathbf{a}^*_{\text{LT}} = [10\bar{1}]^*_\gamma$, $2\mathbf{b}^*_{\text{LT}}$, $2\mathbf{b}^*_{\text{LT}} = \mathbf{q}$, and $\mathbf{c}^*_{\text{LT}} = \frac{1}{3}[222]^*_\gamma$.

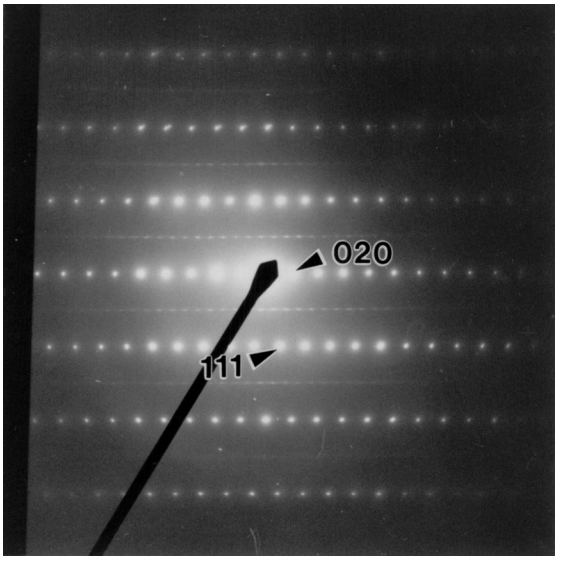


**FIG. 3.** ED from a crystallite of the LT-$Ca_4Bi_6O_{13}$ phase oriented along the $\langle 101\rangle_{LT}$ zone axis. Note the weak (and streaked) additional satellite reflections occurring at the $\mathbf{G}_{LT} \pm \frac{1}{2}\langle 111\rangle^*$ positions of reciprocal space.

additional satellite reflections were indeed observed (see Fig. 3) but they occur at the $\mathbf{G}_{LT} \pm \frac{1}{2}\langle 111\rangle^*$, rather than at the $\mathbf{G}_{LT} \pm \frac{1}{2}\langle 001\rangle^*$, positions of reciprocal space.

While it thus appears that the fine details of the reported single crystal structure refinement (i.e., the weak modulation of the $\mathbf{a}_{LT} = 5.9$, $\mathbf{b}_{LT} = 17.3$, and $\mathbf{c}_{LT} = 3.6$ Å subcell) are not correct, the low value of the obtained refinement statistics shows that the average subcell structure has been refined correctly. For the purposes of this paper, where our prime interest is in the average cation packing, the fine structural detail represented by the observed $\mathbf{G}_{LT} \pm \frac{1}{2}\langle 111\rangle^*$ satellite reflections is unimportant. Its structural significance will be addressed elsewhere (Withers and Larsson, in preparation). (The possibility that the supercell obtained may be dependent upon the method of synthesis should also be kept in mind given that the single crystals of $Ca_4Bi_6O_{13}$ used in the single crystal X-ray study (12) were grown via a synthesis technique different from those used in the present study.)

### *The Relationship between the Reciprocal Lattices of LT-$Ca_4Bi_6O_{13}$ and ss$\gamma$*

While at first glance there appears to be no relationship at all between the reciprocal space lattices of LT-$Ca_4Bi_6O_{13}$ and the quenched ss$\gamma$ phase, this is most certainly not the case as is clear from a careful comparison of Figs. 2a and 2e with Fig. 2c and Figs. 2b and 2f with Fig. 2d. Indeed there is a subset of the strong Bragg reflections of both phases (labeled $\mathbf{G}_{s/c}$ in what follows) which are in common (cf. the outlined reciprocal space "unit cell" in Fig. 2a with that in Fig. 2c and that in Fig. 2b with that in Fig. 2d). This hexagonal reciprocal space supercell is defined by $\mathbf{a}^*_{s/c} = [0\bar{1}1]^*_\gamma = [\bar{1}50]^*_{LT}$, $\mathbf{b}^*_{s/c} = [1\bar{1}0]^*_\gamma = [150]^*_{LT}$, and $\mathbf{c}^*_{s/c} = [222]^*_\gamma = [003]^*_{LT}$, respectively. Note that $2\mathbf{b}^*_{LT}$ therefore corresponds exactly to $\mathbf{q} = \frac{1}{5}[1\bar{2}1]^*_\gamma$.

In real space the above reciprocal space relationships are equivalent to $\mathbf{a}_{s/c} = \frac{1}{3}[\bar{1}\bar{1}2]_\gamma = \frac{1}{10}[\bar{5}10]_{LT}$, $\mathbf{b}_{s/c} = \frac{1}{3}[2\bar{1}\bar{1}]_\gamma = \frac{1}{10}[510]_{LT}$, and $\mathbf{c}_{s/c} = \frac{1}{6}[111]_\gamma = \frac{1}{3}[001]_{LT}$, respectively. These relationships in turn imply that $\mathbf{a}_{LT} = \mathbf{a}_\gamma - \mathbf{c}_\gamma$, $\mathbf{b}_{LT} = \frac{5}{3}(\mathbf{a}_\gamma - 2\mathbf{b}_\gamma + \mathbf{c}_\gamma)$, and $\mathbf{c}_{LT} = \frac{1}{2}(\mathbf{a}_\gamma + \mathbf{b}_\gamma + \mathbf{c}_\gamma)$. An XRPD determined bcc, ss$\gamma$ unit cell parameter $a_\gamma$ *of* 4.25 Å therefore implies LT unit cell parameters of $a_{LT} = 6.01$, $b_{LT} = 17.35$, and $c_{LT} = 3.68$ Å. The XRPD determined LT cell parameters are $a_{LT} = 5.94$, $b_{LT} = 17.37$, and $c/2 = c_{LT} = 3.61$ Å, respectively. This very good agreement is clearly no accident and is the real space analogue of the above statement that there is a subset of the strong Bragg reflections of both phases which are in common.

In addition to this common set of supercell reflections $\mathbf{G}_{s/c}$, there is a further significant similarity in the reciprocal lattices of the quenched ss$\gamma$ phase and the LT phase. This is most clearly seen via a comparison of $\langle 111\rangle_\gamma$ zone axis EDPs with $\langle 001\rangle_{LT}$ zone axis EDPs (compare Figs. 2a and 2e with Fig. 2c). The tendency of the diffuse scattering in the quenched ss$\gamma$ phase to condense out in the vicinity of the $\mathbf{G}_\gamma \pm \mathbf{q}$, $\mathbf{q} \sim 0.2\langle 121\rangle_{\gamma^*}$, positions of reciprocal space (see Figs. 2e and 2f) means that $\langle 111\rangle_\gamma$ zone axis EDPs can be indexed by $\mathbf{H} = \mathbf{G}_{s/c} + m\mathbf{q}$, where $m = 0, \pm 1$ and $\mathbf{q} \approx \frac{1}{5}\langle 1\bar{2}1\rangle_{\gamma^*} = \frac{1}{5}\langle 11\bar{2}0\rangle_{s/c^*}$. In the case of the LT phase, the equivalent $[001]_{LT}$ zone axis EDP (see Fig. 2c) can similarly be indexed as $\mathbf{H} = \mathbf{G}_{s/c} + m\mathbf{q}$, where $m =$ an integer and $\mathbf{q} = 2\mathbf{b}^*_{LT} = \frac{1}{5}[1\bar{2}1]^*_\gamma = \frac{1}{5}[11\bar{2}0]^*_{s/c}$.

The ubiquitous tendency of the diffuse scattering in the ss$\gamma$ phase to condense out in the vicinity of the $\mathbf{G}_\gamma \pm \mathbf{q}$, $\mathbf{q} \sim 0.2\langle 121\rangle^*_\gamma$, positions of reciprocal space (see Figs. 2e and 2f) coupled with the existence of strong Bragg reflections of the LT phase at rather similar positions in reciprocal space (see Figs. 2c and 2d) suggests the possibility that the real space structural modulation responsible for these particular "satellite" reflections may well be related and provides a plausible potential explanation as to the structural origin of the strongest diffuse scattering features in the quenched ss$\gamma$ phase.

While this $\mathbf{q}_1 = 2\mathbf{b}^*_{LT} = \frac{1}{5}[1\bar{2}1]^*_\gamma = \frac{1}{5}[11\bar{2}0]^*_{s/c}$ modulation is apparently in common for both the quenched ss$\gamma$ and LT phases, there exist other "modulations" of the common supercell which are not (compare Figs. 2b and 2f with Fig. 2d). In the case of the quenched ss$\gamma$ phase, for example, there exists a $\mathbf{q}_2 = \frac{1}{3}[11\bar{2}1]^*_{s/c} = [101]^*_\gamma$ "modulation" which does not occur in the LT phase. Similarly, in the case of the LT phase, there exists a $\mathbf{q}_2 = \frac{1}{3}[0001]^*_{s/c} = [001]^*_{LT}$ modulation which does not occur in the case of the quenched ss$\gamma$ phase. Thus the LT phase cannot be described as a modulated variant of the ss$\gamma$ phase or vice versa. Both,

however, can, at least formally, be expressed as modulated variants of the common supercell defined by the above reciprocal space relationships.

In addition to the tendency of the diffuse scattering characteristic of the quenched ss$\gamma$ phase to condense out at specific positions in reciprocal space, it is important to note that it is also characterized by diffuse streaking along reciprocal lattice directions perpendicular to the $\langle 111\rangle_\gamma$ directions of real space; e.g., consider the diffuse streaking along the $\langle 110\rangle_\gamma^*$ directions of reciprocal space in Figs. 1a and 1c, along the $\langle 32\bar{1}\rangle_\gamma^*$ directions of reciprocal space in Figs. 1b and 1d, and along the $\langle 1\bar{2}1\rangle_\gamma^*$ directions of reciprocal space in Figs. 2b and 2f. Such diffuse streaking implies the existence of diffuse sheets of intensity perpendicular to the $\langle 111\rangle_\gamma$ directions of real space which in turn implies the existence of $\langle 111\rangle_\gamma$ columns of atoms whose motion tends to be strongly correlated along $\langle 111\rangle_\gamma$ but uncorrelated in orthogonal directions. The absence of diffuse streaking along the $\langle 1\bar{1}0\rangle_\gamma^*$ directions of reciprocal space in Figs. 2a and 2e further suggests that the direction of motion of the $\langle 111\rangle_\gamma$ columns of atoms responsible for this diffuse streaking is polarized and also largely along the $\langle 111\rangle_\gamma$ real space direction (14).

### *Real Space Relationship between the LT-$Ca_4Bi_6O_{13}$ and ss$\gamma$ Phases*

In the anti $\alpha$-AgI structure reported for the ss$\gamma$ phase (10), the Ca and Bi ions are disordered and distributed on the 000 and $\frac{1}{2}\,\frac{1}{2}\,\frac{1}{2}$ sites of the *Im*3*m*, bcc average structure. Since the reported distribution of the oxygens on an *R*3*m* array was based on an incorrect assumption (10) as shown by electron diffraction methods, no reliable information as to the ordering of the oxygen ions can currently be considered to exist. Given that the contribution of the metal ions will certainly dominate the observed scattering, our focus in what follows is on the average cation positions. Attention will be drawn to the similarity of the cation arrays of the ss$\gamma$ and the LT phases and a suggestion will be made that the strongest diffuse scattering features of the quenched ss$\gamma$ phase are due to the existence of short-range metal ion ordering. The coordinates for the cation positions of the LT-$Ca_4Bi_6O_{13}$ structure are taken from Parise *et al.* (12).

A $\langle 111\rangle_\gamma$ projection of the cation positions ($Ca^{2+}$ and $Bi^{3+}$ disordered) in the bcc ss$\gamma$ phase is shown in Fig. 4a. The cubic stacking sequence is ABCA and the heights of the atoms along the projection axis are 0, $\frac{1}{3}$, and $\frac{2}{3}$, respectively, as shown in the orthogonal $\langle 10\bar{1}\rangle_\gamma$ projection of Fig. 4b. The arrows at the top of Fig. 4b emphasize the existence of $\langle 111\rangle_\gamma$ rods or columns of metal ions which are common to both phases. The observed sheets of diffuse intensity perpendicular to the $\langle 111\rangle_\gamma$ directions in the case of the quenched ss$\gamma$ phase suggests that these metal ion columns move as more or less rigid units along the $\langle 111\rangle_\gamma$ directions. The

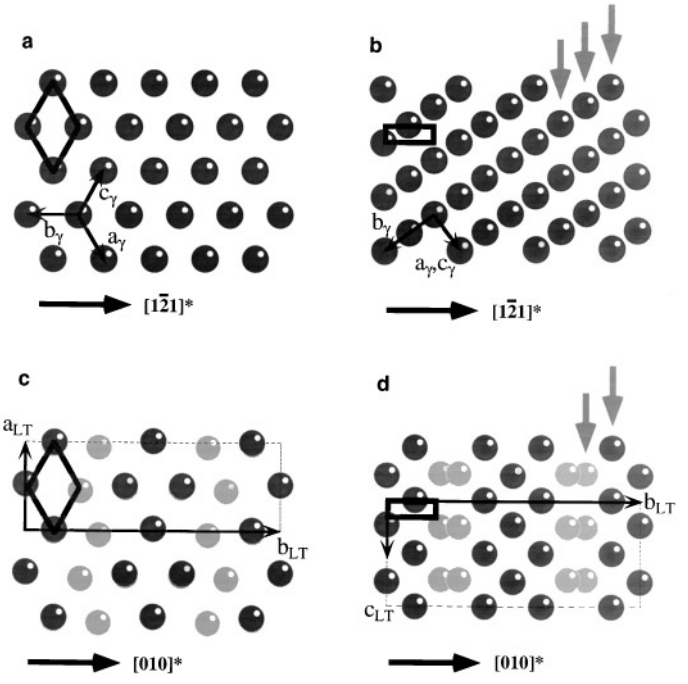


**FIG. 4.** (a), (b), (c), and (d) show the real space projections of the cation arrays corresponding to the zone axis of the EDP in Fig. 2a, 2b, 2c, and 2d, respectively. In (a) and (b), the black disks correspond to the disordered Ca/Bi sites in the ss$\gamma$ structure. In (c) and (d) the grey and black disks correspond to the Ca and Bi ions of the LT-$Ca_4Bi_6O_{13}$ phase, respectively. The common hexagonal "subcell" (cf. text) in the two structures are outlined. Note the similarity between the $\langle 111\rangle_\gamma$ projection of the ss$\gamma$ structure in (a) and the $\langle 001\rangle_{LT}$ projection of the LT-$Ca_4Bi_6O_{13}$ structure in (c). The ordering of Ca/Bi sites in the LT phase cause the strong modulation of the average lattice (i.e., every fifth $\langle 1\bar{2}1\rangle_\gamma$ plane is identical). The other difference between the ss$\gamma$ structure in (b) and LT-$Ca_4Bi_6O_{13}$ structure in (d) is the heights of the close packed atoms rows along the arrows. In ss$\gamma$, the relative heights are 0, $\frac{1}{3}$, and $\frac{2}{3}$ while in the LT phase there are only two relative heights, 0 and $\frac{1}{2}$. (Hence there is no cubic sublattice in the LT phase.)

average crystal structure can be viewed as being formed of layers of these columns of metal ions stacked along a $\langle 1\bar{2}1\rangle_\gamma$ direction.

In Fig. 4c the LT-$Ca_4Bi_6O_{13}$ structure is drawn ($Ca^{2+}$ and $Bi^{3+}$ ions now fully ordered) in projection along $\langle 001\rangle_{LT}$. The same projected hexagonal array of cations as that in the bcc ss$\gamma$ phase is apparent (compare Fig. 4c with 4a). The orthogonal $[100]_{LT}$ projection of Fig. 4d shows the existence of the same layers of columns of metal ions as those that exist in the ss$\gamma$ phase (arrowed). The relative heights of these columns of metal ions along $\mathbf{c}_{LT}$, however, are 0 and $\frac{1}{2}$ rather 0, $\frac{1}{3}$, and $\frac{2}{3}$ (compare Fig. 4d with Fig. 4b).

The metal ion separation distance along the columns of metal ions is very similar for the two structures (3.68 Å for the ss$\gamma$ phase and, on average, $\frac{c}{2} = 3.61$ Å for the LT phase) while the inter-column separation distances in projection along either $\langle 111\rangle_\gamma$ or $[001]_{LT}$ are also very similar (3.47 Å

in the case of the ss$\gamma$ phase compared to 3.44 Å $= \frac{1}{10}[510]_{LT}$ and 3.47 Å $= \frac{1}{5}[050]_{LT}$ for the LT phase). Taken in conjunction with the diffraction evidence that $\langle 111\rangle_\gamma$ columns move as more or less rigid units along the $\langle 111\rangle_\gamma$ direction in the ss$\gamma$ phase, the ease with which it is possible to transform the quenched ss$\gamma$ phase into the LT phase is not surprising.

The difference in the relative heights of the metal ion columns of the two cation arrays is, however, an important difference between the two structure types. The metal ion columns of the LT phase are shifted along the $[001]_{LT}$ projection axis relative to their position in the bcc ss$\gamma$ phase such that the resulting positions of the cations are no longer compatible with bcc symmetry. In the ss$\gamma$ phase there exist four symmetry equivalent sets of ($\langle 111\rangle_\gamma$) metal ion columns. In the LT phase, only one such set (along $[001]_{LT}$) remains intact.

What is the effect of the real space modulation/s of the common supercell (outlined in Figs. 4a–4d) which are *not* in common for the two phases? In the case of the quenched ss$\gamma$ phase, the $\mathbf{q}_2 = \frac{1}{3}[11\bar{2}\bar{1}]^*_{s/c} = [101]^*_\gamma$ "modulation" is clearly responsible for the resultant rhombohedral packing of the metal ion columns apparent in Fig. 4b. In the case of the LT phase, the $\mathbf{q}_2 = \frac{1}{3}[0001]^*_{s/c} = [001]^*_{LT}$ modulation destroys the $\frac{1}{3}c_{LT}$ repeat distance of the supercell and is responsible for the resultant $c_{LT}$ repeat distance.

In the case of the LT phase (as apparent from Figs. 4c and 4d), the $\mathbf{q}_1 = 2\mathbf{b}^*_{LT} = \frac{1}{5}[11\bar{2}0]^*_{s/c}$ modulation has two coupled components—the first is Ca/Bi metal ion ordering and the second is very specific associated changes in the heights of the $[001]_{LT}$ metal ion rods (see Fig. 4d). While the observed diffuse streaking characteristic of the quenched ss$\gamma$ phase provides some evidence for motion of $\langle 111\rangle_\gamma$ metal ion rods along $\langle 111\rangle_\gamma$, there can be no question that the average cation array of the quenched ss$\gamma$ structure still remains bcc (see Figs. 2b and 2f).

The real space structural modulation of the average bcc, cation array associated with the modulation wave vectors $\mathbf{q} \sim 0.23\langle 1\bar{2}1\rangle^*_\gamma$ can then only be due to Ca/Bi ordering and associated structural relaxation. In the case of $M$ = Sr, the primary modulation wave vectors associated with Bi/M cation ordering are apparently commensurable (or locked in) with respect to the average structure. This is presumably responsible for the small metrical distortion of the underlying average structure from cubic to tetragonal (7). In the case of $M$ = Ca, however, the $\mathbf{q} \approx 0.2\langle 1\bar{2}1\rangle^*_\gamma$ primary modulation wave vectors are incommensurable with respect to the underlying bcc average structure. Comparing the real space structures in Fig. 4, the diffuse intensity in the $\mathbf{G}_\gamma \pm \mathbf{q}$, $\mathbf{q} \approx 0.2\langle 1\bar{2}1\rangle^*_\gamma$, regions of reciprocal space of the ss$\gamma$ phase can now be traced back to a periodic compositional modulation along $\langle 1\bar{2}1\rangle^*_\gamma$ of the average concentration of Ca and Bi ions in the arrowed (see Fig. 4b) layers of metal ion columns.

*Annealing Experiments*

Since the diffuse scattering characteristic of the quenched ss$\gamma$ phase has been traced back to metal ion ordering, the next question was to ask if this diffuse scattering is characteristic of the ss$\gamma$ phase itself at elevated temperature or if the existence of the diffuse scattering reflects some (limited) diffusion of ions in the crystal during the quenching procedure. Unfortunately it is not possible to conduct the ED experiment at the elevated temperatures required. Several series of annealing experiments were therefore performed in an attempt to obtain more insight into the ordering process. In one series, the ss$\gamma$ phase was annealed within the temperature range of the ss$\gamma$ solid solution (the samples of the ss$\gamma$ phase in the literature and in our previous experiments were made by quenching from the melt). Stronger diffuse scattering in these annealed samples would have indicated that the diffuse scattering was characteristic of the ss$\gamma$ phase itself. No evidence for any difference between the original samples and these annealed samples, however, could be found either in PXRD or ED data.

The quenched ss$\gamma$ phase was then annealed at various different temperatures *within the temperature range of existence of the LT phase*. With time and temperature optimized, it was found that such annealing did indeed increase the intensity and sharpness of the observed diffuse scattering markedly (see Figs. 1 and 2). Samples were annealed at between 300 and 700°C for selected times. At 700°C the LT phase was formed within a few minutes. As would be expected, the minimum annealing time before the phase transition to the LT phase occurred increased gradually with decreased temperature. The intensity and sharpness of the observed diffuse scattering was found to increase with annealing time at any one temperature. For example, 10 min annealing at 500°C gave rise to the EDPs in Figs. 1c and 1d and 2e and 2f. This suggests that the metal ion ordering characteristic of the ss$\gamma$ phase is rather short-range ordered at elevated temperatures but susceptible to being increased upon appropriate annealing.

Even if the two types of EDPs, from the quenched sample and from the quenched and then annealed sample, are clearly very similar, they are not identical. The diffuse maxima of the electron scattering in the ss$\gamma$ phase have turned into sharp satellite reflections in the annealed sample and the positions of these maxima have changed slightly. Additionally, while the diffuse scattering in the as quenched ss$\gamma$ sample is stronger on the *high* angle side of the Bragg reflections, it is stronger on the *low* angle side of the Bragg reflections in the annealed sample. This is referred to as the "atomic size effect" (15) and could possibly in this case be connected to the degree of order. However, with the limited information available on the details of the atomic positions in the ss$\gamma$ phase no further conclusions can at this stage be drawn from this effect.

## DISCUSSION

An important question to ask in order to understand these ternary bismuth oxides and their oxygen ion conductivity properties is why the cation rods are shifted in the LT phase relative to their positions in the ss$\gamma$ phase. The LT structure has been described in terms of C-shaped double ribbons of edge-shared $BiO_5$ square pyramids linked by $Bi_2O_5$ groups (12). Parise *et al.* (12) pointed out that the same triangular $BiO_3$ arrangement as in this $Bi_2O_5$ group is found in new high-temperature superconductors and in this context it is tempting to speculate about the importance of this $Bi_2O_5$ group in the formation of the LT phase. The stereochemically active lone pairs of electrons associated with $Bi^{3+}$ ions clearly play an important role in stabilizing these C-shaped structural units while at higher temperatures the effect of the stereochemically active lone pairs is less pronounced. The symmetry of the $Bi_2O_5$ groups constrain the $BiO_5$ square pyramids in the neighboring rods to be at the same relative height along **c**. It is hence clear that the presence of this C-shaped structural unit is not compatible with the underlying cubic symmetry of the bcc cation array. Unfortunately, the structural details of this $Bi_2O_5$ group could not be sufficiently well resolved from the refinement of the single crystal X-ray data set used by Parise *et al.* (12). However, since the EDPs of the LT phase showed a modulation wave vector different from the one used for their refinements, it is feasible that further investigation of the LT phase may result in more information as to the crystal chemical significance of this $Bi_2O_5$ group.

## ACKNOWLEDGMENTS

Financial support for AKL from STINT via the Swedish Natural Science Research Council (NFR) is gratefully acknowledged.

## REFERENCES

1. T. Takahashi, H. Iwahara, and Y. Nagai, *J. Appl. Electrochem.* **2,** 97–104 (1972).
2. T. Takahashi and H. Iwahara, *Mater. Res. Bull.* **13,** 1447 (1978).
3. A. J. Burggraaf, T. Van Dijk, and M. J. Verkerk, *Solid State Ionics* **5,** 519 (1981).
4. T. Graia, P. Conflant, G. Nowogrocki, J. C. Boivin, and D. Thomas, *J. Solid State Chem.* **63,** 160–165 (1986).
5. P. Conflant, J.-C. Boivin, and D. Thomas, *J. Solid State Chem.* **18,** 133–140 (1976).
6. L. G. Sillen and B. Sillen, *Z. Phys. Chem.* **49B,** 27–33 (1944).
7. R. Guillermo, P. Conflant, J.-C. Boivin, and D. Thomas, *Rev. Chim. Min.* **15,** 153–159 (1978).
8. F. Honnart, J. C. Boivin, D. Thomas, and E. J. de Vries, *Solid State Ionics* **9&10,** 921 (1983).
9. U. Delicat, K. Gruber, A. Püttner, E. J. Zehnder, and M. Trömel, *J. Solid State Chem.* **102,** 209–212 (1993).
10. K. Gruber, P. Hofer, M. Tromel, H. Fuess, and M. Pinot, *J. Solid State Chem.* **108,** 250–252 (1994).
11. M. O'Keeffe and B. G. Hyde, *Structure Bonding* **61,** 77–144 (1985).
12. J. B. Parise, C. C. Torardi, M.-H. Whangbo, C. J. Rawn, R. S. Roth, and B. P. Burton, *Chem. Mater.* **2,** 454–458 (1990).
13. R. S. Roth, C. J. Rawn, B. P. Burton, and F. Beech, *Abst. Am. Crystallogr. Assoc.* **2, 17,** 41 (1989).
14. T. R. Welberry, *Rep. Prog. Phys.* **48,** 1543–1593 (1985).
15. T. R. Welberry, *J. Appl. Crystallogr.* **19,** 382–389 (1986).